Neural Networks 144 (2021) 455–464

Contents lists available at ScienceDirect

Neural Networks

journal homepage: www.elsevier.com/locate/neunet

Detection of pancreatic cancer by convolutional-neural-network-assisted spontaneous Raman spectroscopy with critical feature visualization

Zhongqiang Li [a], Zheng Li [a], Qing Chen [c], Alexandra Ramos [b], Jian Zhang [c], J. Philip Boudreaux [d], Ramcharan Thiagarajan [d], Yvette Bren-Mattison [d], Michael E. Dunham [e], Andrew J. McWhorter [e], Xin Li [a], Ji-Ming Feng [b], Yanping Li [f], Shaomian Yao [b], Jian Xu [a,*,1]

[a] Division of Electrical and Computer Engineering, College of Engineering, Louisiana State University, Baton Rouge, LA 70803, USA
[b] Department of Comparative Biomedical Science, School of Veterinary Medicine, Louisiana State University, Baton Rouge, LA 70803, USA
[c] Division of Computer Science & Engineering, College of Engineering, Louisiana State University, Baton Rouge, LA 70803, USA
[d] Department of Surgery, School of Medicine, Louisiana State University Health Science Center, New Orleans, LA 70112, USA
[e] Department of Otolaryngology, School of Medicine, Louisiana State University Health Science Center, New Orleans, LA 70112, USA
[f] School of Environment and Sustainability, University of Saskatchewan, Saskatoon, SK S7N 5C9, Canada

ARTICLE INFO

Article history:
Received 25 May 2021
Received in revised form 23 August 2021
Accepted 3 September 2021
Available online 16 September 2021

Keywords:
Deep learning
Pancreatic cancer
Convolutional neural network
Spontaneous Raman spectroscopy
Lab-designed hand-held Raman spectroscopic system

ABSTRACT

Pancreatic cancer is the deadliest cancer type with a five-year survival rate of less than 9%. Detection of tumor margins plays an essential role in the success of surgical resection. However, histopathological assessment is time-consuming, expensive, and labor-intensive. We constructed a lab-designed, hand-held Raman spectroscopic system that could enable intraoperative tissue diagnosis using convolutional neural network (CNN) models to efficiently distinguish between cancerous and normal pancreatic tissue. To our best knowledge, this is the first reported effort to diagnose pancreatic cancer by CNN-aided spontaneous Raman scattering with a lab-developed system designed for intraoperative applications. Classification based on the original one-dimensional (1D) Raman, two-dimensional (2D) Raman images, and the first principal component (PC1) from the principal component analysis on the 2D image, could all achieve high performance: the testing sensitivity, specificity, and accuracy were over 95%, and the area under the curve approached 0.99. Although CNN models often show great success in classification, it has always been challenging to visualize the CNN features in these models, which has never been achieved in the Raman spectroscopy application in cancer diagnosis. By studying individual Raman regions and by extracting and visualizing CNN features from max-pooling layers, we identified critical Raman peaks that could aid in the classification of cancerous and noncancerous tissues. 2D Raman PC1 yielded more critical peaks for pancreatic cancer identification than that of 1D Raman, as the Raman intensity was amplified by 2D Raman PC1. To our best knowledge, the feature visualization was achieved for the first time in the field of CNN-aided spontaneous Raman spectroscopy for cancer diagnosis. Based on these CNN feature peaks and their frequency at specific wavenumbers, pancreatic cancerous tissue was found to contain more biochemical components related to the protein contents (particularly collagen), whereas normal pancreatic tissue was found to contain more lipids and nucleic acid (particularly deoxyribonucleic acid/ribonucleic acid). Overall, the CNN model in combination with Raman spectroscopy could serve as a useful tool for the extraction of key features that can help differentiate pancreatic cancer from a normal pancreas.

1. Introduction

Pancreatic cancer is the fourth most prominent cause of cancer deaths in the United States (US). Its five-year survival rate is ∼9% for all stages combined, and only 3% for patients in the advanced stage (Pandya, et al., 2008; Society, 2020). According to recent statistics published by the American Cancer Association, there were 57,600 new cases of pancreatic cancer diagnosed in 2020 alone and 47,050 deaths. Pancreatic cancer has the highest ratio of new death/new cases at 81.68% (Society, 2020). In clinical practice, surgical resection is the primary treatment approach for the removal of pancreatic cancer at an early stage. If surgery fails

* Corresponding author.
E-mail address: jianxu1@lsu.edu (J. Xu).
[1] Jian Xu's orcid: orcid.org/0000-0002-6595-8602.

https://doi.org/10.1016/j.neunet.2021.09.006
0893-6080/

to resect cancer completely, the resection site is subject to local relapse. Rapid intraoperative differentiation of cancer and normal tissue plays an essential role in achieving complete resection of pancreatic cancer (Yang, et al., 2014).

To date, several common approaches have been used for the detection of pancreatic cancer, such as computerized tomography, magnetic resonance imaging, and positron emission tomography. However, most of these techniques are time-consuming, expensive, require bulky equipment, and are unsuitable for intraoperative tissue diagnosis with sufficient sensitivity and specificity. The most common method of tissue diagnosis is the postsurgical histological examination of tumor specimens (Yang, et al., 2014). However, this procedure typically takes several hours to days to acquire the final diagnostic report, and the accuracy of such an analysis relies heavily on the sample quality, experience of the pathologist, and medical procedures (Pandya, et al., 2008; Society, 2020).

Raman spectroscopy is an emerging, real-time diagnostic tool for analyzing chemical components with unique advantages, including nondestructive examination, no sample preparation, and high specificity to the chemical components (Boiret, Rutledge, Gorretta, Ginot, & Roger, 2014; Kourkoumelis, et al., 2015; Pence & Mahadevan-Jansen, 2016). Raman spectroscopy has been extensively used in many fields, including chemistry, food, environmental science, and medicine (Boiret et al., 2014; He, et al., 2018; Notingher, et al., 2004; Sato-Berru, et al., 2007; Xu, Gao, Han, & Zhao, 2017). Moreover, it has been previously used to diagnose cancers, such as oral, skin, breast cancers, brain cancer (Gebrekidan, et al., 2018; Ghosh, et al., 2019; Kourkoumelis, et al., 2015; Manoharan, et al., 1998). To explore the potential features from the spectral data, the most common methods for the classification of Raman signals are principal component analysis (PCA), linear discriminant analysis, and support vector machines (SVMs) (Sohn, Lee, & Kim, 2020).

However, the identification of critical Raman features using the above-mentioned methods is generally time-consuming and labor-intensive. For example, Raman spectra are processed by PCA in groups. This results in low efficiency in data usage, and many important features cannot be easily identified manually from other PCA components or scatter plots (Boyaci, et al., 2014; Pandya, et al., 2008; Stone, Kendall, Shepherd, Crow, & Barr, 2002; Uy & O'Neill, 2005). In comparison with the conventional methods (e.g., PCA), deep learning does not require manual intervention to extract Raman features, and has now been successfully applied in many medical fields, such as electrocardiographic (ECG) analysis and tumor segmentation in medical images (Al Rahhal, et al., 2016; Havaei, et al., 2017; Kowal, Skobel, Gramacki, & Korbicz, 2021; Zhao, et al., 2018). The convolutional neural network (CNN) is one of the most successful deep learning models, and exhibits several advantages, including the requirement of little prior knowledge or design of explicit features, and a strong capability to capture inner structures (Fan, Ming, Zeng, Zhang, & Lu, 2019; Liu, et al., 2017; Lussier, Thibault, Charron, Wallace, & Masson, 2020; Peng, Zheng, Li, Yang, & Deng, 2020). Some existing studies have already demonstrated that using Raman spectroscopy in combination with deep learning approaches could be an optimal strategy for the diagnosis of cancer or analysis of photoinduced DNA damage (Erzina, et al., 2020; Hollon, et al., 2020; Weng, Xu, Li, & Wong, 2017; Zhang, et al., 2019). However CNN models are still difficult to visualize critical Raman features (peak information) from CNN representations, even most of them could achieve excellent performance in distinguishing different tissue types (Fukuhara, Fujiwara, Maruyama, & Itoh, 2019). The role of recognizing spectral features (particularly peak information) from CNN features is critical in the identification of biomolecular components (Fukuhara et al., 2019). Our study represents the first effort in this field to extract critical CNN Raman features that aid in the diagnosis of pancreatic cancer. In addition, to the best of our knowledge, this is also the first study that adopts CNN-aided spontaneous Raman spectroscopy for pancreatic cancer diagnosis.

Thus far, in most existing studies, 1D Raman has been used directly as a dataset for CNN classification (Carvalho, et al., 2017; Lee, Lenferink, Otto, & Offerhaus, 2019; Shao, et al., 2020). However, the single Raman data cannot directly perform the prefeature extraction by using PCA. If the individual Raman spectrum could be converted into a 2D Raman image, then each new 2D image could utilize PCA for some prefeature extraction. Our study not only evaluates 1D Raman but also explores the efficiency of 2D Raman images obtained from the dot products of 1D Raman. This study also extracts and visualizes the hidden CNN features from max-pooling layers.

2. Materials and methods

2.1. Animals and Raman spectroscopy system

In this study, the human CFPAC-1 cell line (ATCC® CRL-1918™, pancreatic ductal adenocarcinoma) was used. Before the injection of the cells in an animal host, tumor cells were grown in Iscove's Modified Dulbecco's Medium (ATCC® 30-2005™) with 10% fetal bovine serum (Neuromics, Edina, Minnesota) at 37 °C and 5% CO_2 in a humidified environment. For the animal model, we used 6–8-week-old female immunocompetent athymic nude Nu/J mice (stock #002019, Jackson Laboratories, Bar Harbor, Maine, USA).

After the CFPAC-1 cells were incubated in media, approximately 2×10^6 cells were transplanted to the dorsa of the mice by subcutaneous injection. When the size of the tumor was approximately 1 cm, the mice were euthanized, and the entire tumor and normal pancreas were dissected. This study was approved by the Institutional Animal Care and Use Committee of Louisiana State University (IACUC#20-046), and all operations followed the guidelines on animal research.

The Raman spectroscopy system consisted of a 785 nm laser source (laser diode, Turnkey Raman Lasers-785 Series, Ocean Optics Inc., Dunedin, Flurida, United States), QE Pro spectrometer (Ocean Optics, Inc), and a Raman probe (RPS785, InPhotonics Inc., Norwood, Massachusetts, United States). When the Raman spectra were acquired, the Raman probe was fixed behind the specimen at a distance of approximately 5 mm. In this study, 20 mice were used. The entire tumor and normal pancreas were extracted from each mouse. Subsequently, 1305 Raman spectra were collected from the tumor, and 1224 Raman spectra were collected from the pancreas.

2.2. Raman measurements, data processing, and data analysis with CNN models

The measured raw Raman signals often include noise (mainly from tissue autofluorescence), and the real Raman signals require preprocessing before feature extractions (Pandya, et al., 2008). The typical procedures of Raman spectral processing are (1) autofluorescence removal by asymmetric truncated quadratic processing (Mazet, Carteret, Brie, Idier, & Humbert, 2005), (2) background removal, (3) noise removal with the Savitzky–Golay filter (Cordero, et al., 2017), and (4) normalization.

In addition to the original 1D Raman signal, 2D Raman images were also obtained from the dot product of each normalized Raman spectrum and its transpose, as depicted in Fig. 1. To extract the potential features in 2D Raman images, each 2D Raman image was prefeatured by PCA, and the score of the first PCA

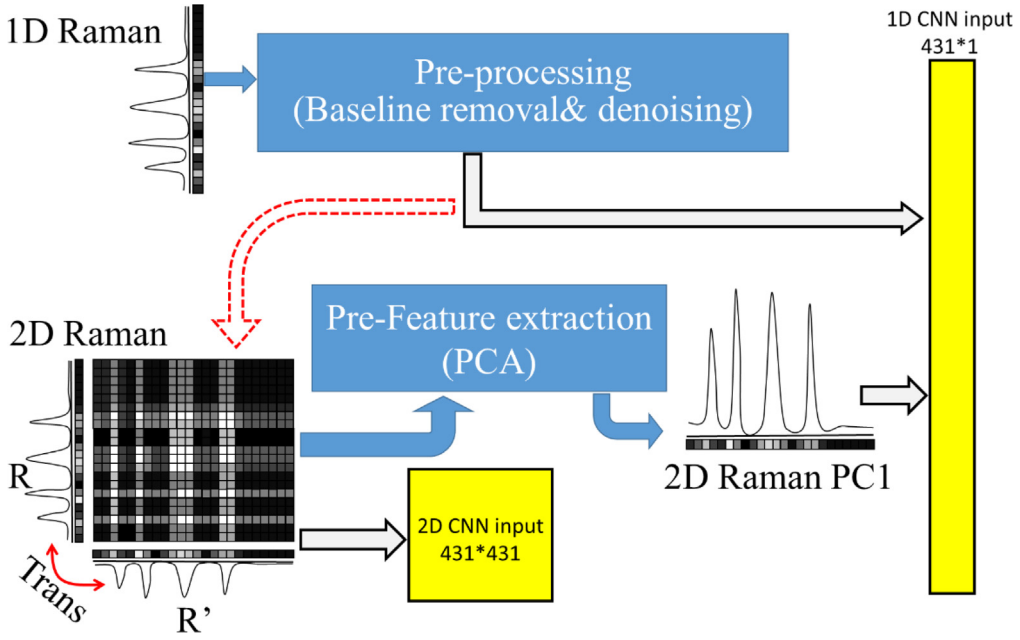

Fig. 1. Data processing of one-dimensional (1D) Raman and two-dimensional (2D) Raman images for the convolutional neural network (CNN) model.

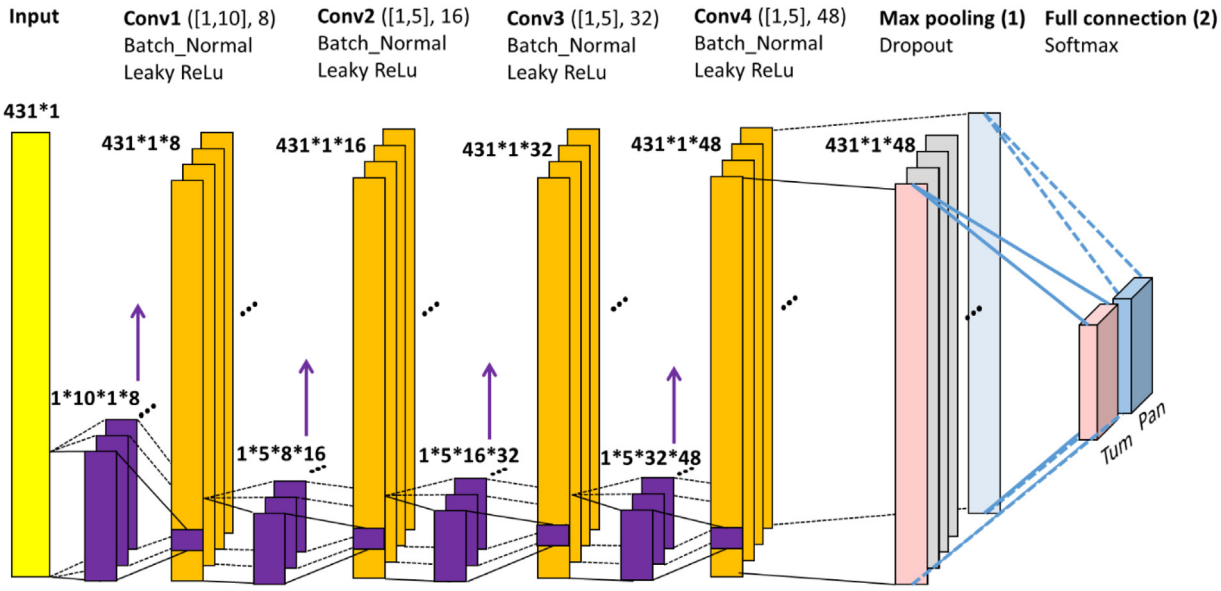

Fig. 2. Schematic of the 1D CNN models used to detect pancreatic cancer in a murine cancer model. To match the visualized CNN features with the corresponding wavenumbers, the stride size was set to 1 to keep the same total length of the feature map in each convolutional (Conv) layer. In the 2D CNN model, all the convolution filters in the 1D CNN were converted into 2D convolution filters; the stride size was changed to 2. All the other configurations were the same as those in the 1D model (Purple blocks: Conv filters; orange blocks: feature maps).. (For interpretation of the references to color in this figure legend, the reader is referred to the web version of this article.)

components (2D Raman PC1) were used as the inputs for CNN models.

We explored two types of CNN models for the classification task: a 1D CNN model, which was used for 1D Raman signals and the 2D Raman PC1, and a 2D CNN model used for the 2D Raman images. The overall structures of these two types of CNN models were the same, and were composed of four convolution layers (Conv), a dropout layer, a max-pooling layer, a full connection layer, and a softmax layer, as illustrated in Fig. 2. For the length of feature maps, when keeping the padding size unchanged, the total length of feature maps will be determined by the stride sizes. To match the extracted CNN features with their corresponding wavenumbers, the stride sizes were set to 1 in each convolutional layer.

Each convolution layer applied convolution to its input, followed by batch normalization (Batch_Normal) and leaky rectified linear unit (ReLu) activation. The filter size of the first convolution layer was set to [1, 10], and the filter size was [1, 5] for the other three subsequent convolution layers. The number of filters was set to 8 for the first convolution layer (Conv1), followed by 16 for the second convolution layer (Conv2), and 32 and 48 for the third and fourth convolution layers, respectively. Five-fold cross-validation was performed to test the CNN models. Sensitivity,

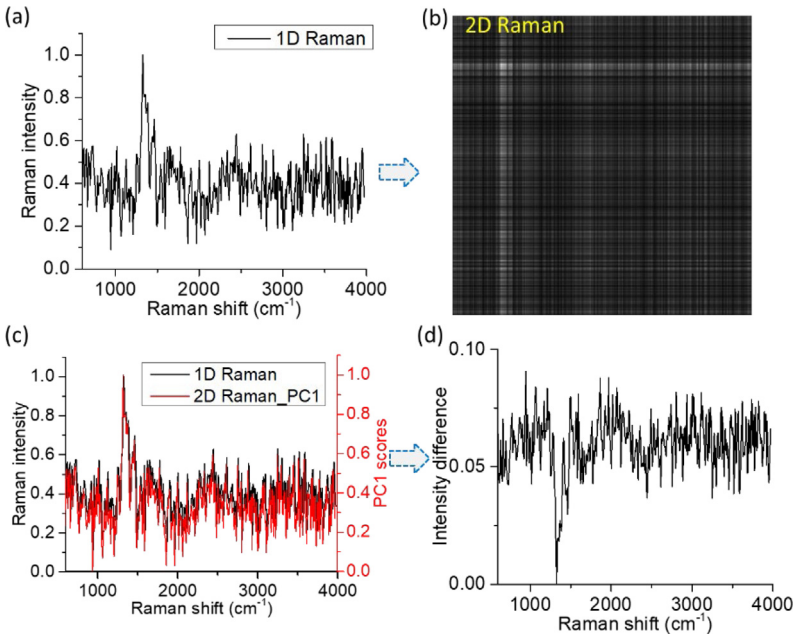

Fig. 3. 1D Raman and 2D Raman images to identify pancreatic cancer. (a) Original 1D Raman spectrum of pancreatic cancer and (b) corresponding 2D Raman images obtained from the dot product of the 1D Raman spectrum and its transpose. (c) Comparison of original 1D Raman spectrum and the normalized 2D Raman PC1 scores. (d) Difference between the original 1D Raman spectrum and the normalized 2D Raman PC1 scores.

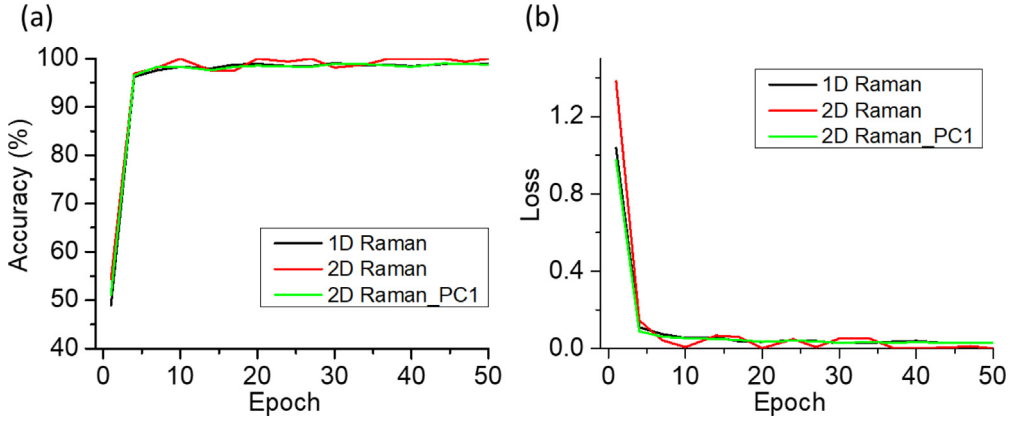

Fig. 4. (a) Accuracy-epoch and (b) loss-epoch curves of 1D Raman, 2D Raman images, and 2D Raman PC1 during CNN training (each curve is the average of five-fold cross-validation, and the learning rate is set to 0.001).

specificity, and accuracy were calculated for the evaluation of the model performance.

In the 2D Raman CNN model, the filter sizes were changed to [10, 10] for the Conv1 layers, and [5, 5] for the other three convolution layers. The configurations of the other layers were maintained similarly to those of the 1D CNN model.

All analyses were conducted with MATLAB (version R2019b, MathWorks Inc, Natick, MA, USA).

3. Results

3.1. 1D and 2D raman images for detection of pancreatic cancer in a mouse model

The typical 1D Raman spectrum obtained from the cancerous pancreatic tissue (Fig. 3a) commonly contained a large peak at approximately 1330 cm^{-1}. The corresponding 2D Raman image exhibited a diagonal symmetry (Fig. 3b). The overall trend of the 1D Raman spectrum and the normalized 2D Raman PC1 were similar. However, most of the troughs in the 2D Raman PC1 were relatively lower than those in the 1D Raman curve at the same Raman shift (by 0.08 on average, Fig. 3d). The largest peak remained unchanged during normalization. Thus, the difference between the peaks and troughs of the Raman spectra was slightly larger in the 2D Raman PC1 than in the 1D Raman spectrum (Fig. 3c).

3.2. Evaluation of a CNN model for detection of pancreatic cancer with 1D and 2D raman images

To evaluate the efficiency of the CNN models in identifying cancerous and normal pancreatic tissues, 80% of the Raman data were used for training, 10% of the data were used for validation, and 10% of the data were used for testing. To train the CNN models based on 1D Raman, 2D Raman image, and 2D Raman PC1 (Fig. 4), each training process contained 50 epochs and used a learning rate of 0.001. Both the 1D and 2D CNN models achieved an accuracy >95% only after 5 epochs of training; the training loss became less than 0.05 after 20 epochs for all three models. After 35 epochs of training, the model based on 2D Raman images

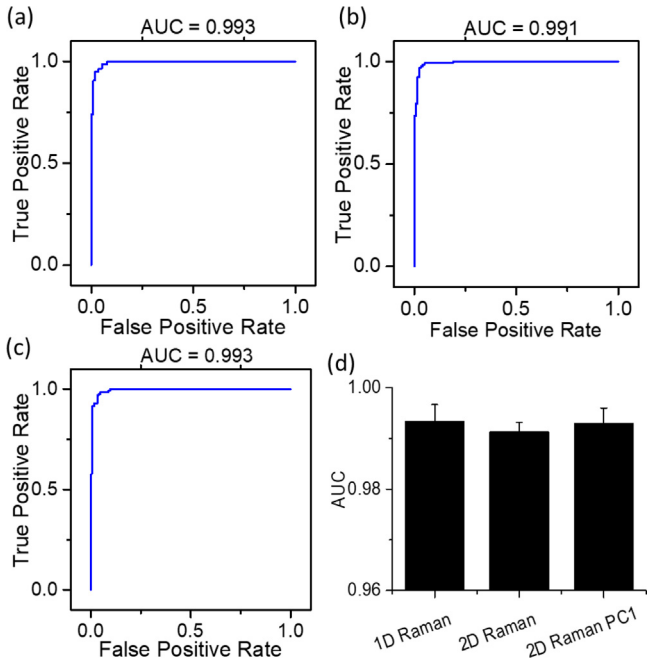

Fig. 5. Receiver operating characteristic curves of (a) 1D Raman model, (b) 2D Raman image model, (c) 2D Raman PC1 model, (d) AUCs of 1D Raman, 2D Raman image and 2D Raman PC1.

yielded lower loss rates (<0.005) than those based on 1D Raman (∼0.04) and 2D Raman PC1 (∼0.03). After 35 epochs, the 2D Raman image model yielded a slightly higher accuracy (close to 100%) than those of the 1D Raman model (98.8%) and 2D Raman PC1 model (98.9%).

Fig. 5 plots the receiver operating characteristic curves of the 1D and 2D CNN models. All three models achieved high performance in the classification of cancerous and normal pancreatic tissues. The areas under the curve (AUCs) were 0.993 ± 0.003 for the 1D Raman and 2D Raman PC1 models, and 0.991 ± 0.002 for the 2D Raman image model (Fig. 5d).

We also gathered statistical measures of the CNN model performance (Fig. 6). All the CNN models demonstrated excellent accuracy, sensitivity, and specificity. The 1D Raman (97.39 ± 1.44%) and 2D Raman PC1 (96.60 ± 1.21%) CNN models yielded slightly better accuracy than that of the 2D Raman image (96.44 ± 0.48%) CNN model. The 1D Raman (97.80 ± 0.90%) CNN models yielded similar sensitivities to those of the 2D Raman PC1 (97.67 ± 1.81%) and 2D Raman image (97.67 ± 1.65%) CNN models. The 2D Raman PC1 (95.56 ± 0.85%) and the 1D Raman (96.85 ± 2.52%) models exhibited slightly better specificity than that of the 2D Raman image model (95.15 ± 1.63%). Thus, the CNN models could efficiently distinguish between cancerous and normal pancreatic tissues through the Raman spectra. All three models exhibited similar and high efficiencies.

3.3. Visualization of the CNN hidden features from the max-pooling layer

Although CNN was successful in differentiating species by Raman signals, it is still challenging to identify the key Raman features that help with this differentiation. A recent study was conducted to visualize the Raman features from max-pooling layers to differentiate between pharmaceutical compounds and numerically mixed amino acids. (Fukuhara et al., 2019). In this study, we explored the feasibility of visualization of hidden Raman features in differentiating between cancerous and normal tissues from max-pooling layers.

The mean Raman spectra of the 1D Raman and 2D Raman PC1 of the cancerous and normal pancreatic tissues were loaded in their corresponding trained CNN classifiers; the strongest activation channels were then extracted from the max-pooling layers. Given that the sizes of the feature maps in each convolution layer were the same as those of the input features, the visualized CNN features were plotted with the Raman shifts, and some critical CNN Raman features were visualized from the max-pooling layers. In the 1D Raman CNN model (Fig. 7a), the Raman peaks at 720 and 1660 cm^{-1} were more significant in the normal pancreas, whereas the peaks at 1449 cm^{-1} were considerably higher in the cancerous pancreas. In the 2D Raman PC1 CNN model, more peaks could be extracted. The peaks at 645, 821, 855, 1243, 1449, and 1583 cm^{-1} (Fig. 7b) were only found in pancreatic cancer, whereas the peaks at 671 cm^{-1} were more significant in the normal pancreas.

The mean 2D Raman images of the cancerous and normal pancreatic tissues were also loaded in the trained 2D CNN classifier. The CNN features were then extracted from the max-pooling layer and reshaped to the original size of the input 2D Raman images. On the reconstructed 2D images, the R1 region was relatively brighter in pancreatic cancer; however, this area was darker for the normal pancreas (Fig. 8a Tum-R1 vs. Pan-R1). In contrast, the R2 region was relatively darker for the cancerous pancreas but brighter in the normal pancreas (Fig. 8a Tum-R2 vs. Pan-R2).

From the plot of the normalized diagonal pixel values, it can be seen that the normal pancreas had a lower intensity than the cancerous pancreas when the Raman shift was lower than 1800 cm^{-1}. This tendency was reversed when the Raman shift was beyond this value. In the wavenumber range of 600–1800 cm^{-1}, the peaks at 1128 and 1449 cm^{-1} could be found on the diagonal pixel curve for the cancerous pancreas (red line: Tum_diagnol), and a 1010 cm^{-1} peak was found on that for the normal pancreas (black line: Pan_diagnol) (Fig. 8b).

Similar to Fig. 7, all the strongest activation channels of the test dataset (visualized CNN features) were extracted and visualized from the max-pooling layers across 10-fold cross-validation. The Raman spectra with the correct classification were selected and their mean CNN feature curves are depicted in Fig. 9. In 2D Raman PC1 (Fig. 9b), the Raman spectra in the wavenumber range of 600–1800 cm^{-1} exhibited larger intensities than those beyond 1800 cm^{-1}, whereas 1D Raman exhibited slightly larger Raman intensities in the range of 600–1600 cm^{-1} (Fig. 9a). This result was more evident in the full wavenumber range (600–3970 cm^{-1}) (Fig. S2). Pancreatic cancer (red line) yielded substantial peaks at 623, 727, 821, 855, 1449, 1583, and 1640 cm^{-1} in the 1D Raman spectra (Fig. 9a), and the peaks at 623, 727, 855, 1128, 1177, 1449, and 1640 cm^{-1} in the 2D Raman PC1 (Fig. 9b). The normal pancreas (black line) yielded detectable peaks at 720, 1100, 1258, 1482, and 1744 cm^{-1} in the 1D Raman spectra, and 720, 1010, 1100, 1258, 1482, 1575, and 1744 cm^{-1} in the 2D Raman PC1.

We also studied the frequency of Raman peaks of visualized CNN features that appeared across all the tested spectra. In 1D Raman, 623, 727, 821, 855, 1449, 1583, 1620, and 1640 cm^{-1} appeared frequently for pancreatic cancer, whereas 720, 1100, 1258, 1482, and 1744 cm^{-1} were frequently found for the normal pancreas (Fig. 10a). In 2D Raman PC1, peaks with high peak frequency could be observed at 623, 727, 855, 1177, 1449, 1555, and 1620 cm^{-1} in pancreatic cancer, and at 720, 1010, 1100, 1258, and 1744 cm^{-1} in the normal pancreatic tissue (Fig. 10b).

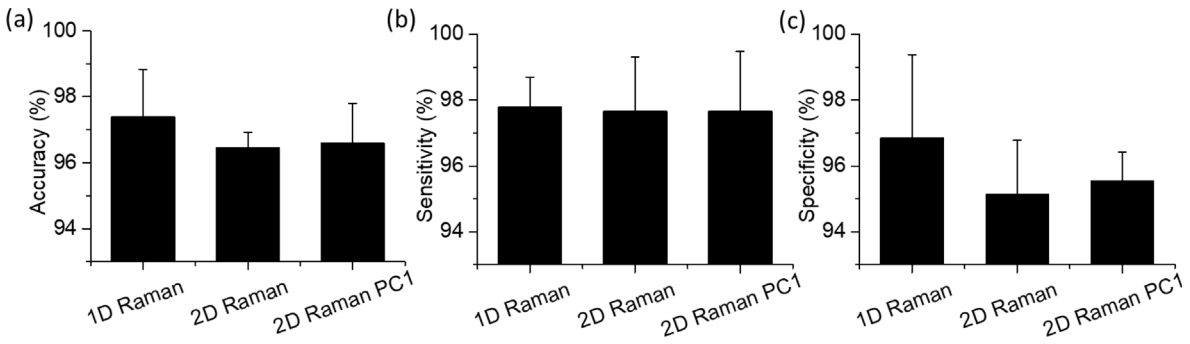

Fig. 6. (a) Accuracy, (b) sensitivity, and (c) specificity of the 1D and 2D CNN models used for the distinction between cancerous and normal pancreatic tissues.

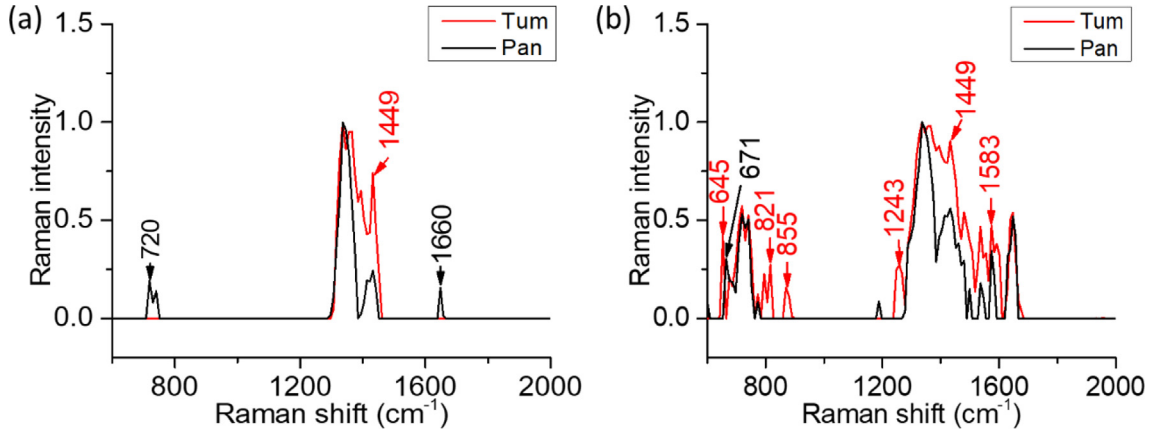

Fig. 7. CNN features of the mean spectra of cancerous pancreatic tissue and normal pancreatic tissue; CNN features were the strongest activations extracted from the max-pooling layer in (a) 1D Raman and (b) 2D Raman PC1.

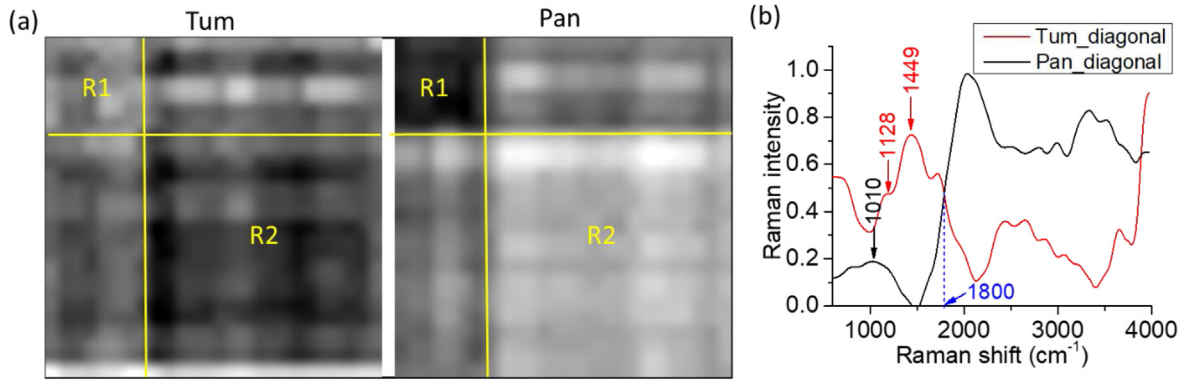

Fig. 8. CNN features from the max-pooling layer in the mean 2D Raman images. (a) 2D images of CNN features of cancerous (Tum) and normal pancreatic (Pan) tissues from the max-pooling layer. (b) Normalized diagonal pixel curves from 2D images of CNN features.

3.4. Screening frequency regions important for accurate pancreatic cancer detection using CNN models

To examine the contribution of each wavelength region to the classification, we divided the full wavenumber range (600–3970 cm^{-1}) into 215 individual subregions, each being 22 cm^{-1} wide. The subregions were then loaded individually into the 1D CNN model to differentiate between a pancreatic tumor and a normal pancreas. Fig. 11 depicts the testing accuracy of each individual subregion. The subregions of 848–869, 1056–1077, 1346–1400, 1546–1565, 1720–1760, and 1790–1810 cm^{-1} were found to contribute higher accuracy in classifying tissues using the 2D Raman PC1 CNN model. The subregions of 1178–1198, 2010–2027, 2195–2211, 3011–2025, 3510–3540, 3620–3650, and 3917–3940 cm^{-1} resulted in higher tissue classification accuracies using the 1D Raman CNN model.

4. Discussion

Pancreatic cancer deaths are ranked fourth among all cancer deaths in the US with a low five-year survival rate (≤9%). Thus far, there has been no reliable method to rapidly differentiate between cancerous and normal tissues (e.g., <1 min) (Pandya, et al., 2008; Society, 2020). In this study, we designed highly effective CNN models to differentiate between cancerous and normal pancreatic tissues based on Raman spectroscopy. To further utilize the hidden Raman signal features for the CNN models, we constructed 2D Raman images from the original 1D Raman

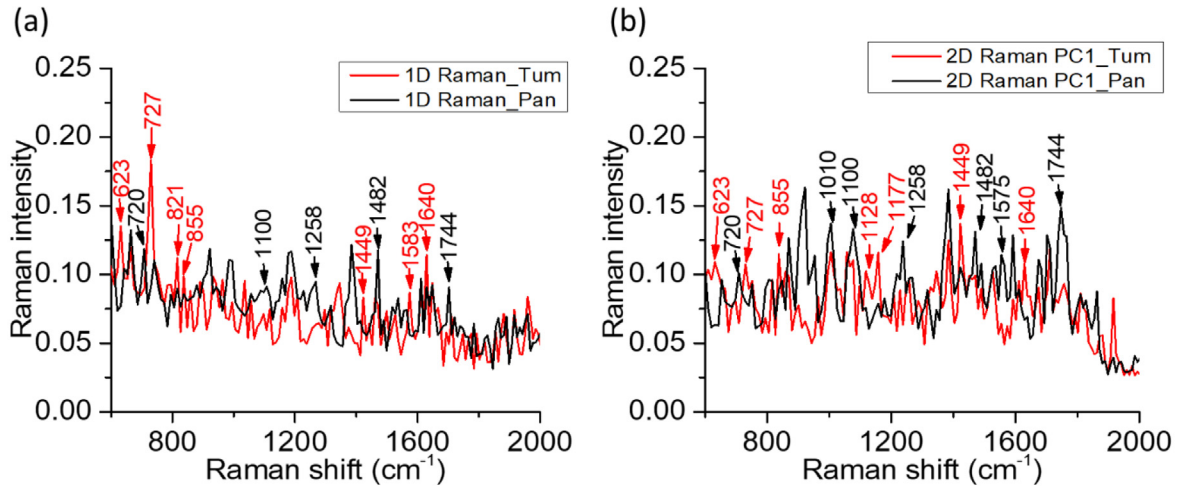

Fig. 9. Mean CNN feature curves of the test dataset from the max channels of the max-pooling layers in the wavenumber range of 600–2000 cm^{-1}. (a) 1D Raman and (b) 2D Raman PC1 (Tum: pancreatic cancer, Pan: normal pancreas).. (For interpretation of the references to color in this figure legend, the reader is referred to the web version of this article.)

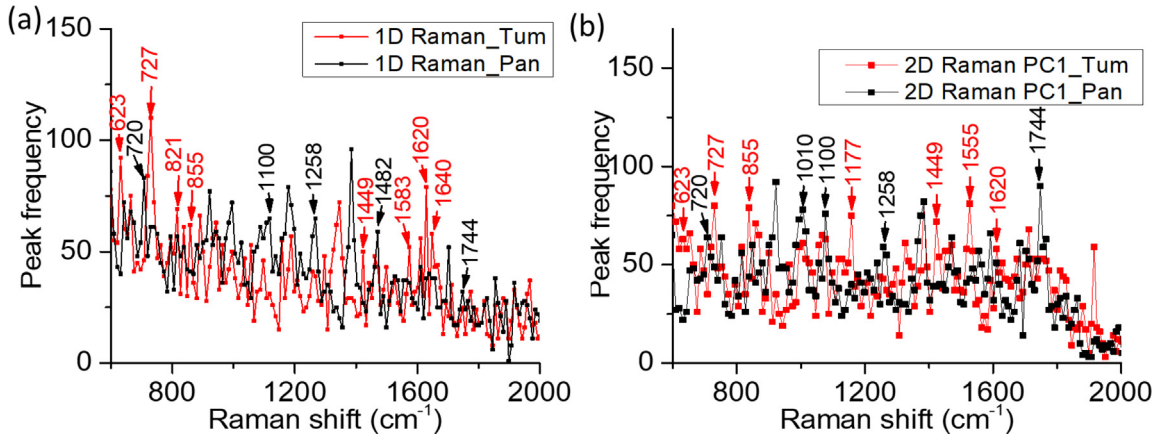

Fig. 10. Peak frequency at specific wavenumbers occurring in the CNN features of the test dataset from the max channels of the max-pooling layers. (a) 1D Raman and (b) 2D Raman PC1. Peak intensity >0.5, like in Fig. 7.

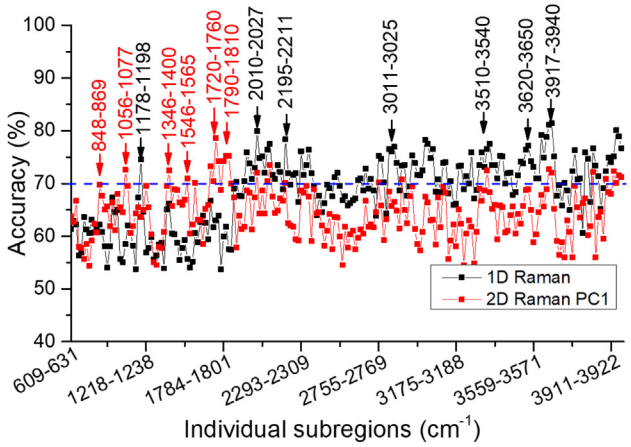

Fig. 11. Accuracies of individual subregions of 1D Raman and 2D Raman PC1 in classifying cancerous and normal pancreatic tissues.

spectra by the dot products of the Raman spectra and their transposes. Additionally, each 2D Raman image was processed by PCA to generate 2D Raman PC1 data. Compared with the original 1D Raman spectrum, 2D Raman PC1 could enlarge the difference between the maximum and minimum values of the signal. 1D Raman, 2D Raman images, and 2D Raman PC1 were then loaded into 1D or 2D CNN models to classify cancerous and normal pancreatic tissues.

All three methods could achieve excellent performance in classifying cancerous and normal pancreatic tissues, where the training accuracies were over 98.8% and the training losses were smaller than 0.05. Compared with 1D Raman and 2D Raman PC1, the model that used 2D Raman images could acquire a slightly higher training accuracy (close to 100%) and a considerably lower training loss (less than 0.005). From the test dataset, it can be seen that all three methods yielded high-testing accuracy (>96%), sensitivity (>97%), and specificity (>95%) in the identification of cancerous and noncancerous Raman spectra. In the three cases, AUC could reach up to 0.99. Thus, the CNN model with four convolutional layers has high efficiency in classifying cancerous and normal pancreatic tissues.

When compared to the conventional GoogLeNet model (being revised for 1D and 2D Raman signals) and random forest, our proposed CNNs model exhibits a better efficiency for the classification of pancreatic cancer with about 2% higher than GoogleNet in accuracy, sensitivity, and specificity (Fig. S3 and S4), when up to 5% higher than the random forest in accuracy and specificity.

Moreover, due to the complicated architectures of GoogleNet, the whole training procedures cost a large amount of time (over 2,600s for 1D Raman spectra and around 1,100s for 2D images). However, our proposed CNNs only take about 60 s (1D Raman) for a single 50-epochs training due to the simple structures, and the accuracy is higher than the convolutional architecture. Meanwhile, we also examine the influence of the number of the convolutional layers on the classification of pancreatic cancer. The results show that our proposed CNNs with 4 convolutional layers is an optimal design for the classification of pancreatic cancer; under three datasets, the testing accuracy, sensitivity, and specificity of our proposed CNN models were larger than the similar CNNs with 3 or 5 convolutional layers (Fig. S5).

Currently, gross examination, intraoperative frozen section analysis (IFSA), and postsurgical histopathological examinations are the most common approaches used for the evaluation of pancreatic cancer (Ghosh, et al., 2019; Handgraaf, et al., 2014; Yang, et al., 2014; Zhou, et al., 2012). However, these conventional methods have significant drawbacks and are incompatible with the accurate intraoperative diagnosis because they are (1) time-consuming (e.g. postsurgical histopathological examinations > 20–30 min), (2) highly subjective to histopathological translation, (3) dependent on tissue preparation (particularly in IFSA), (4) are associated with a limited number of biopsy points, and (5) associated with sampling bias and tissue loss owing to biopsies (Jaafar, 2006; Pandya, et al., 2008; Society, 2020; Vahini, Ramakrishna, Kaza, & Murthy, 2017). Compared with these traditional approaches, Raman signals are strongly dependent on the changes of chemical compositions (e.g., proteins or nucleic acids) in the biological samples. Raman peak positions and amplitudes contain important biochemical information on tissue compositions (Sohn et al., 2020). Therefore, identifying the critical Raman peaks or regions that help differentiate cancerous from noncancerous tissues is crucial in the understanding of the chemical composition changes among various tissues. Many studies have reported that using a CNN model in combination with Raman spectra could serve as a satisfactory, rapid, and non-destructive approach to classify chemical species (Fan et al., 2019; Mazet et al., 2005; Ralbovsky & Lednev, 2020).

However, visualization and interpretation of the critical features from the CNN model remains the main challenge of this approach. In the field of CNN-aided Raman spectroscopy, there was only one recent report that used simple spectra, generated by the Lorentzian function and white noise, to aid in the feature visualization of amino acids and pharmaceutical compounds mixed with known ratios (Fukuhara et al., 2019). Our work is the first report in this field to identify the critical Raman features that can assist in the classification of cancerous and noncancerous tissues. We extracted the maximum activation channels from max-pooling layers to visualize the critical features that are most relevant to the classification by CNN models. In addition, to the best of our knowledge, our effort is also the first CNN-aided spontaneous Raman spectroscopy study to provide intraoperative pancreatic cancer diagnosis.

Based on the accuracy of the screening regions (Fig. S1), it was found that the Raman regions of 600–1800 cm^{-1} (fingerprint region Lee et al., 2019) are important for the classification of cancerous and normal pancreatic tissues. This result was further confirmed by the max-pooling features of mean 2D images (Fig. 8) and the mean CNN feature curves of the test dataset (Fig. 9). In the fingerprint region (600–1800 cm^{-1}), the mean 1D Raman and 2D Raman PC1 (Fig. 7) yielded peaks at 645, 821, 855, 1243, 1449, and 1583 cm^{-1}, which were indicative of pancreatic cancer, whereas the 720 and 1660 cm^{-1} peaks were relevant to a normal pancreas. Thus, both 1D Raman and 2D Raman PC1 helped visualize their unique CNN features for the classification of cancerous and normal pancreatic tissues.

In addition, the CNN features from the entire test dataset provided more critical feature visualization. 2D Raman PC1 yielded larger peak magnitudes in CNN features than those in 1D Raman. In the CNN features of the test dataset and their high-frequency peaks, the Raman peaks at 623, 727, 821, 855, 1128, 1177, 1449, 1555, 1583, 1620, and 1640 cm^{-1} were found in pancreatic cancer, whereas the peaks at 720, 1010, 1100, 1258, 1482, 1575, and 1744 cm^{-1} were found in the normal pancreas.

Given that Raman peaks are strongly related to chemical components, the visualized CNN features listed above and the high-frequency peaks indicative of pancreatic cancer are more likely to be linked with the peaks of 623, 645, 727, 821, 855, 1128, 1177, 1243, 1449, 1555, 1583, 1620, and 1640 cm^{-1} that represent protein components, particularly collagen contents (Casper, 1993; Chan, et al., 2006; Cheng, Liu, Liu, & Lin, 2005; Dawson, Rueda, Aparicio, & Caldas, 2013; Frank, McCreery, & Redd, 1995; Frank, Redd, Gansler, & McCreery, 1994; Lau, et al., 2003; Pandya, et al., 2008; Schulz & Baranska, 2007; Talari, 2015). The normal pancreas yields distinct peaks at 671, 720, 1010, 1100, 1258, 1482, 1575, and 1744 cm^{-1}, indicating the components of lipids and nucleic acid (particularly DNA/RNA) (Casper, 1993; Notingher, et al., 2004; Pandya, et al., 2008); (Stone, Kendall, Smith, Crow, & Barr, 2004; Talari, 2015). Thus, this method can aid in the analysis of biomolecular tissue components through chemical analysis, and pancreatic cancerous tissue can be rapidly identified by its Raman features.

5. Conclusions

In this study, we designed CNN models that could efficiently classify cancerous and normal pancreatic tissue based on spontaneous Raman spectra, which was the first such effort in the application of pancreatic cancer diagnosis. The original 1D Raman and the two 2D Raman methods could achieve high performance: testing sensitivity, specificity, and accuracy were higher than 95%, and the AUC could be up to 0.99. Through the screening of increasing regions and individual subregions and the visualization of CNN features, the fingerprint regions (600–1800 cm^{-1}) were significant to the recognition of pancreatic cancer. With the CNN features extracted from max-pooling layers, we located some Raman peaks that were critical to the classification of cancerous and normal tissue. From these peaks, we could identify that the cancerous pancreatic tissue contained increased protein content, particularly collagen, whereas the normal pancreas contained more lipids and nucleic acid (particularly DNA/RNA). This was the first effort that visualized features in the field of CNN-aided Raman spectroscopy for cancer diagnosis. Overall, the CNN model, in combination with spontaneous Raman spectroscopy, could serve as a useful tool for the extraction of key features that can aid in the differentiation of pancreatic cancerous tissue from a normal pancreas.

Although our work has demonstrated the feasibility of pancreatic cancer detection by CNN-assisted spontaneous Raman scattering and the possibility of important Raman feature visualization from CNN models for the first time in this field, the current study was limited to murine cancer models. The findings will be evaluated further in conjunction with human pancreatic cancer studies in the near future. Moreover, our CNN-aided spontaneous Raman spectroscopy, with our lab-designed Raman system, has the potential to become a rapid (<30 s), accurate tool for intraoperative tissue diagnosis in pancreatic cancer surgery.

CRediT authorship contribution statement

Zhongqiang Li: CNN model design, Data acquisition, Analysis, Interpretation, Drafted the manuscript. **Zheng Li:** Data acquisition, Analysis, Interpretation, Drafted the manuscript. **Qing Chen:** CNN model improvement, Data acquisition, Interpretation, Drafted the manuscript. **Alexandra Ramos:** Data analysis, Interpretation, Drafted the manuscript. **Jian Zhang:** CNN model improvement, Data interpretation, Proofread the manuscript. **J. Philip Boudreaux:** Data acquisition, Proofread the manuscript. **Ramcharan Thiagarajan:** Data acquisition, Proofread the manuscript. **Yvette Bren-Mattison:** Data acquisition, Proofread the manuscript. **Michael E. Dunham:** Data interpretation, Proofread the manuscript. **Andrew J. McWhorter:** Data interpretation, Proofread the manuscript. **Xin Li:** Data interpretation, Revision of the manuscript. **Ji-Ming Feng:** Data interpretation, Revision of the manuscript. **Yanping Li:** Data analysis, Revision of the manuscript. **Shaomian Yao:** Data interpretation, Revision of the manuscript. **Jian Xu:** Conception, Experimental design, Data interpretation, Critical revision of the manuscript.

Declaration of competing interest

The authors declare that they have no known competing financial interests or personal relationships that could have appeared to influence the work reported in this paper.

Acknowledgments

This research was supported by Louisiana State University, USA Economic Development Assistantships (000398), LSU Leveraging Innovation for Technology Transfer (LIFT2) Grant (LSU-2021-LIFT-009, LSU-2020-LIFT-008), Health Sciences Center New Orleans, USA, Louisiana State University, USA Grant (HSCNO-2019-LIFT-004), Louisiana Board of Regents Grant, USA (LEQSF (2018-21)-RD-A-09, LEQSF(2020-21)-RD-D-02), National Science Foundation (NSF), USA CAREER award (2046929).

Appendix A. Supplementary data

Supplementary material related to this article can be found online at https://doi.org/10.1016/j.neunet.2021.09.006.

References

Al Rahhal, M. M., Bazi, Y., AlHichri, H., Alajlan, N., Melgani, F., & Yager, R. R. (2016). Deep learning approach for active classification of electrocardiogram signals. *Information Sciences*, *345*, 340–354.

Boiret, M., Rutledge, D. N., Gorretta, N., Ginot, Y.-M., & Roger, J.-M. (2014). Application of independent component analysis on Raman images of a pharmaceutical drug product: pure spectra determination and spatial distribution of constituents. *Journal of Pharmaceutical and Biomedical Analysis*, *90*, 78–84.

Boyaci, I. H., Temiz, H. T., Uysal, R. S., Velioglu, H. M., Yadegari, R. J., & Rishkan, M. M. (2014). A novel method for discrimination of beef and horsemeat using Raman spectroscopy. *Food Chemistry*, *148*, 37–41.

Carvalho, L. F. C., Bonnier, F., Tellez, C., Dos Santos, L., O'Callaghan, K., O'Sullivan, J., et al. (2017). Raman spectroscopic analysis of oral cells in the high wavenumber region. *Experimental and Molecular Pathology*, *103*, 255–262.

Casper, E. S. (1993). Pancreatic cancer: How can we progress? *European Journal of Cancer*, *29*, 171–172.

Chan, J. W., Taylor, D. S., Zwerdling, T., Lane, S. M., Ihara, K., & Huser, T. (2006). Micro-Raman spectroscopy detects individual neoplastic and normal hematopoietic cells. *Biophysical Journal*, *90*, 648–656.

Cheng, W. T., Liu, M. T., Liu, H. N., & Lin, S. Y. (2005). Micro-Raman spectroscopy used to identify and grade human skin pilomatrixoma. *Microscopy Research and Technique*, *68*, 75–79.

Cordero, E., Korinth, F., Stiebing, C., Krafft, C., Schie, I. W., & Popp, J. (2017). *Evaluation of Shifted Excitation Raman Difference Spectroscopy and Comparison to Computational Background Correction Methods Applied to Biochemical Raman Spectra. Sensors (Basel), 17*.

Dawson, S. J., Rueda, O. M., Aparicio, S., & Caldas, C. (2013). A new genome-driven integrated classification of breast cancer and its implications. *EMBO Journal*, *32*, 617–628.

Erzina, M., Trelin, A., Guselnikova, O., Dvorankova, B., Strnadova, K., Perminova, A., et al. (2020). Precise cancer detection via the combination of functionalized SERS surfaces and convolutional neural network with independent inputs. *Sensors and Actuators B (Chemical)*, *308*.

Fan, X., Ming, W., Zeng, H., Zhang, Z., & Lu, H. (2019). Deep learning-based component identification for the Raman spectra of mixtures. *Analyst*, *144*, 1789–1798.

Frank, C. J., McCreery, R. L., & Redd, D. C. (1995). Raman spectroscopy of normal and diseased human breast tissues. *Analytical Chemistry*, *67*, 777–783.

Frank, C. J., Redd, D. C., Gansler, T. S., & McCreery, R. L. (1994). Characterization of human breast biopsy specimens with near-IR Raman spectroscopy. *Analytical Chemistry*, *66*, 319–326.

Fukuhara, M., Fujiwara, K., Maruyama, Y., & Itoh, H. (2019). Feature visualization of Raman spectrum analysis with deep convolutional neural network. *Analytica Chimica Acta*, *1087*, 11–19.

Gebrekidan, M. T., Erber, R., Hartmann, A., Fasching, P. A., Emons, J., Beckmann, M. W., et al. (2018). Breast tumor analysis using shifted-excitation Raman difference spectroscopy (SERDS). *Technology in Cancer Research & Treatment*, *17*, Article 1533033818782532.

Ghosh, A., Raha, S., Dey, S., Chatterjee, K., Roy Chowdhury, A., & Barui, A. (2019). Chemometric analysis of integrated FTIR and Raman spectra obtained by non-invasive exfoliative cytology for the screening of oral cancer. *Analyst*, *144*, 1309–1325.

Handgraaf, H. J., Boonstra, M. C., Van Erkel, A. R., Bonsing, B. A., Putter, H., Van De Velde, C. J., et al. (2014). Current and future intraoperative imaging strategies to increase radical resection rates in pancreatic cancer surgery. *BioMed Research International*, *2014*.

Havaei, M., Davy, A., Warde-Farley, D., Biard, A., Courville, A., Bengio, Y., et al. (2017). Brain tumor segmentation with deep neural networks. *Medical Image Analysis*, *35*, 18–31.

He, S., Fang, S., Xie, W., Zhang, P., Li, Z., Zhou, D., et al. (2018). Assessment of physiological responses and growth phases of different microalgae under environmental changes by Raman spectroscopy with chemometrics. *Spectrochimica Acta Part A: Molecular and Biomolecular Spectroscopy*, *204*, 287–294.

Hollon, T. C., Pandian, B., Adapa, A. R., Urias, E., Save, A. V., Khalsa, S. S. S., et al. (2020). Near real-time intraoperative brain tumor diagnosis using stimulated Raman histology and deep neural networks. *Nature Medicine*, *26*, 52–58.

Jaafar, H. (2006). Intra-operative frozen section consultation: concepts, applications and limitations. *The Malaysian Journal of Medical Sciences: MJMS*, *13*, 4.

Kourkoumelis, N., Balatsoukas, I., Moulia, V., Elka, A., Gaitanis, G., & Bassukas, I. D. (2015). Advances in the in Vivo Raman spectroscopy of malignant skin tumors using portable instrumentation. *International Journal of Molecular Sciences*, *16*, 14554–14570.

Kowal, M., Skobel, M., Gramacki, A., & Korbicz, J. (2021). Breast cancer nuclei segmentation and classification based on a deep learning approach. *International Journal of Applied Mathematics and Computer Science*, *31*.

Lau, D. P., Huang, Z., Lui, H., Man, C. S., Berean, K., Morrison, M. D., et al. (2003). Raman spectroscopy for optical diagnosis in normal and cancerous tissue of the nasopharynx—preliminary findings. *Lasers in Surgery and Medicine*, *32*, 210–214.

Lee, W., Lenferink, A. T. M., Otto, C., & Offerhaus, H. L. (2019). Classifying Raman spectra of extracellular vesicles based on convolutional neural networks for prostate cancer detection. *Journal of Raman Spectroscopy*, *51*, 293–300.

Liu, J., Osadchy, M., Ashton, L., Foster, M., Solomon, C. J., & Gibson, S. J. (2017). Deep convolutional neural networks for Raman spectrum recognition: a unified solution. *Analyst*, *142*, 4067–4074.

Lussier, F., Thibault, V., Charron, B., Wallace, G. Q., & Masson, J.-F. (2020). Deep learning and artificial intelligence methods for Raman and surface-enhanced Raman scattering. *TRAC Trends in Analytical Chemistry*, *124*, Article 115796.

Manoharan, R., Shafer, K., Perelman, L., Wu, J., Chen, K., Deinum, G., et al. (1998). Raman spectroscopy and fluorescence photon migration for breast cancer diagnosis and imaging. *Photochemistry and Photobiology*, *67*, 15–22.

Mazet, V., Carteret, C., Brie, D., Idier, J., & Humbert, B. (2005). Background removal from spectra by designing and minimising a non-quadratic cost function. *Chemometrics and Intelligent Laboratory Systems*, *76*, 121–133.

Notingher, I., Green, C., Dyer, C., Perkins, E., Hopkins, N., Lindsay, C., et al. (2004). Discrimination between ricin and sulphur mustard toxicity in vitro using Raman spectroscopy. *Journal of the Royal Society Interface*, *1*, 79–90.

Pandya, A. K., Serhatkulu, G. K., Cao, A., Kast, R. E., Dai, H., Rabah, R., et al. (2008). Evaluation of pancreatic cancer with Raman spectroscopy in a mouse model. *Pancreas*, *36*, e1-8.

Pence, I., & Mahadevan-Jansen, A. (2016). Clinical instrumentation and applications of Raman spectroscopy. *Chemical Society Reviews*, *45*, 1958–1979.

Peng, G., Zheng, Y., Li, J., Yang, J., & Deng, Z. (2020). Single upper limb pose estimation method based on improved stacked hourglass network. *International Journal of Applied Mathematics and Computer Science*, *31*, 123–133.

Ralbovsky, N. M., & Lednev, I. K. (2020). Towards development of a novel universal medical diagnostic method: Raman spectroscopy and machine learning. *Chemical Society Reviews*, *49*, 7428–7453.

Sato-Berru, R. Y., Mejia-Uriarte, E. V., Frausto-Reyes, C., Villagran-Muniz, M., S, H. M., & Saniger, J. M. (2007). Application of principal component analysis and Raman spectroscopy in the analysis of polycrystalline BaTiO3 at high pressure. *Spectrochimica Acta, Part A (Molecular and Biomolecular Spectroscopy)*, *66*, 557–560.

Schulz, H., & Baranska, M. (2007). Identification and quantification of valuable plant substances by IR and Raman spectroscopy. *Vibrational Spectroscopy*, *43*, 13–25.

Shao, X., Zhang, H., Wang, Y., Qian, H., Zhu, Y., Dong, B., et al. (2020). Deep convolutional neural networks combine Raman spectral signature of serum for prostate cancer bone metastases screening. *Nanomedicine*, *29*, Article 102245.

Society, A. C. (2020). Cancer facts & figures 2020: The society.

Sohn, W. B., Lee, S. Y., & Kim, S. (2020). Single-layer multiple-kernel-based convolutional neural network for biological Raman spectral analysis. *Journal of Raman Spectroscopy*, *51*, 414–421.

Stone, N., Kendall, C., Shepherd, N., Crow, P., & Barr, H. (2002). Near-infrared Raman spectroscopy for the classification of epithelial pre-cancers and cancers. *Journal of Raman Spectroscopy*, *33*, 564–573.

Stone, N., Kendall, C., Smith, J., Crow, P., & Barr, H. (2004). Raman spectroscopy for identification of epithelial cancers. *Faraday Discussions*, *126*, 141–157.

Talari, A. C. S. (2015). *Raman Spectroscopic Analysis to Identify Chemical Changes Associated with Different Subtypes of Breast Cancer Tissue Samples*. University of Sheffield.

Uy, D., & O'Neill, A. E. (2005). Principal component analysis of Raman spectra from phosphorus-poisoned automotive exhaust-gas catalysts. *Journal of Raman Spectroscopy*, *36*, 988–995.

Vahini, G., Ramakrishna, B., Kaza, S., & Murthy, N. (2017). Intraoperative frozen section—A golden tool for diagnosis of surgical biopsies. *International Clinical Pathology Journal*, *4*(00084).

Weng, S., Xu, X., Li, J., & Wong, S. T. (2017). Combining deep learning and coherent anti-Stokes Raman scattering imaging for automated differential diagnosis of lung cancer. *Journal of Biomedical Optics*, *22*, Article 106017.

Xu, M.-L., Gao, Y., Han, X. X., & Zhao, B. (2017). Detection of pesticide residues in food using surface-enhanced Raman spectroscopy: a review. *Journal of Agricultural and Food Chemistry*, *65*, 6719–6726.

Yang, L., Sajja, H. K., Cao, Z., Qian, W., Bender, L., Marcus, A. I., et al. (2014). uPAR-targeted optical imaging contrasts as theranostic agents for tumor margin detection. *Theranostics*, *4*(106).

Zhang, L., Wu, Y., Zheng, B., Su, L., Chen, Y., Ma, S., et al. (2019). Rapid histology of laryngeal squamous cell carcinoma with deep-learning based stimulated Raman scattering microscopy. *Theranostics*, *9*(2541).

Zhao, X., Wu, Y., Song, G., Li, Z., Zhang, Y., & Fan, Y. (2018). A deep learning model integrating FCNNs and CRFs for brain tumor segmentation. *Medical Image Analysis*, *43*, 98–111.

Zhou, Y., Liu, C. H., Sun, Y., Pu, Y., Boydston-White, S., Liu, Y., et al. (2012). Human brain cancer studied by resonance Raman spectroscopy. *Journal of Biomedical Optics*, *17*, Article 116021.